Iron nanoparticles with tunable tetragonal structure and magnetic properties

Jinming Liu,[1] Karl Schliep,[2] Shi-Hai He,[1] Bin Ma,[1] Ying Jing,[1] David J. Flannigan,[2] and Jian-Ping Wang[1,2,*]

[1]*Department of Electrical and Computer Engineering, University of Minnesota, 200 Union Street SE, Minneapolis, Minnesota 55455, USA*

[2]*Department of Chemical Engineering and Materials Science, University of Minnesota, 421 Washington Avenue SE, Minneapolis, Minnesota 55455, USA*

(Received 15 September 2017; revised manuscript received 11 January 2018; published 30 May 2018)

Body-centered cubic (bcc) Fe is known as a typical soft magnetic material with high-saturation magnetization (M_s) and low magnetocrystalline anisotropy. However, first-principles calculations demonstrate that body-centered tetragonal (bct) Fe has higher magnetocrystalline anisotropy than bcc Fe and comparable M_s. In this work, bct Fe nanoparticles (NPs) were successfully fabricated by a gas-phase condensation method for the first time. The bct Fe phase is confirmed by the x-ray diffraction pattern and diffraction images of transmission electron microscopy. An increased magnetocrystalline anisotropy of bct Fe, $(2.65 \pm 0.67) \times 10^5$ J/m^3 [(21.2 ± 5.3) μeV/atom], is observed, which is around seven times higher than that of bcc Fe 4.8×10^4 J/m^3 (3.5 μeV/atom). The bct Fe NPs sample has coercivity of 3.22×10^5 A/m at 5 K and 1.04×10^5 A/m at 300 K, which are much higher than that of bcc Fe NPs. In addition, the saturation magnetization at 5 K is estimated to be $(1.6 \pm 0.4) \times 10^6$ A/m (2.2 ± 0.5 μ_B/atom), comparable to that of bcc Fe 1.7×10^6 A/m (2.2 μ_B/atom).

DOI: 10.1103/PhysRevMaterials.2.054415

I. INTRODUCTION

Magnetic nanoparticles (NPs) that possess a large maximum energy product, $(BH)_{\max}$, have attracted significant attention for their application in permanent magnet (PM) technologies, such as electric motors [1] and wind turbines [2]. Therefore, materials with large magnetic anisotropy energy (MAE) and high-saturation magnetization (M_s) are good candidates for PMs. Rare-earth (RE) PMs have good magnetic performance and thermal stability. However, the socioeconomic supply limitations and high price of RE elements, such as neodymium and dysprosium, stimulate new research on alternative magnetic materials [3,4]. Therefore, new magnetic materials for PMs should be inexpensive and naturally abundant. Current research aims to enhance the MAE in materials that already possess large M_s using structural asymmetry such as tetragonal distortion. One such example is the tetragonal L_{10} phase FePt [5,6]. Despite its suitable magnetic properties, precious metal Pt is not cost effective for broad use. Fe known as a soft magnetic material is attractive because of its small MAE (4.8×10^4 J/m^3) [7], high M_s, and abundant availability on the earth. Even higher M_s of Fe with the metastable Fe_6 phase was reported [8]. Fe should have high magnetic coercivity to obtain large $(BH)_{\max}$. In 2004, Burkert *et al.* predicted the MAE of tetragonal Fe and FeCo could increase by orders of magnitude, while the M_s is still close to body-centered cubic (bcc) Fe and bcc FeCo [9,10]. Therefore, combing high M_s and large MAE, body-centered tetragonal (bct) Fe is a promising candidate for non-rare-earth PMs.

Research on tetragonal Fe first focuses on ultrathin films to investigate the structural and magnetic properties [11–15]. Martin *et al.* point out Fe monolayers on Ir(001) showing thickness-dependent structure properties, where 2-monolayer Fe has face-centered tetragonal (fct) structure and bct structure for 3–10 monolayer Fe [16]. However, no experimental results report large MAE of bct Fe. However, experimental results on bct FeCo thin film and core-shell nanoparticles (bct FeCo shell with AuCu core) indicate that bct FeCo has high MAE and M_s, which are consistent with theoretical predictions [17,18]. Experimental investigation of bct Fe and FeCo are on strained thin films or strained core-shell structures. Thus, the strong demagnetization field may conceal the MAE, which may hinder the further characterization and understanding of those new materials. As a result, NP samples with single magnetic domain are desirable for both fundamental magnetic research and technological applications such as PMs.

In order to prepare bct Fe NPs, the Fe phase diagram is investigated at first. According to the low-pressure phase diagram of pure Fe [19], face-centered cubic (fcc) γ-Fe is stable at high temperatures (between 910 °C and 1394 °C) and bcc α-Fe at low temperatures (below 910 °C). Compared to bcc α-Fe, fcc γ-Fe can be treated as a distorted bcc α-Fe with a c axis stretched to $c/a = \sqrt{2}$. Therefore, according to the Bain path, a metastable bct Fe should exist as an intermediate phase between fcc γ-Fe and bcc α-Fe [20]. In our gas-phase condensation (GPC) method, the NPs always evolve from a high-temperature phase to a low-temperature phase due to the plasma heating effects [21,22]. In order to get the intermediate bct Fe, Fe NPs need to be quenched at the intermediate stage before they evolve into the stable bcc phase. Therefore, properly controlled quenching is a critical requirement to prepare bct Fe NPs.

In this work, bct Fe NPs were prepared for the first time by a GPC system. The plasma heating effect of the GPC system is modulated by sputter current, magnetic field, and gas flow rate to achieve a proper quenching requirement for the formation

*Author to whom correspondence should be addressed: jpwang@umn.edu

of bct Fe. The bct Fe NPs exhibit a magnetic coercivity of 3.22×10^5 A/m at 5 K and 1.04×10^5 A/m at 300 K and MAE $\sim (2.65 \pm 0.67) \times 10^5$ J/m^3 [$(21.2 \pm 5.3)\,\mu$eV/atom] with M_s comparable to that of bcc Fe.

II. EXPERIMENTAL DETAILS

Fe NPs were synthesized using a magnetron-sputtering-based gas-phase condensation (GPC) system. The GPC system was shown in Fig. 1, containing a source chamber and a deposition chamber connected by a small aperture. A two-inch high-purity Fe planer target (99.95%) was used to fabricate Fe NPs. In order to prepare NPs, a much higher sputtering pressure (350 mTorr) is used [23,24]. Such a high sputtering pressure can greatly increase the collision rate between the sputtered atoms and Ar atoms, and the energy of the sputtered atoms transfers to Ar atoms and then the sputtered atoms are cooled down followed by NP nucleation and growth [25,26]. During the fabrication process, the sputtering current was varied from 0.2 A to 0.6 A. The pressure in the source chamber was kept as 350 mTorr by ultrahigh-purity argon gas, while the pressure in the deposition chamber was below 1 mTorr to create a pressure differential between the source chamber and deposition chamber. Due to this pressure differential, an argon gas flow was formed from the source chamber to the deposition chamber. The synthesized Fe NPs were carried by argon gas flow to the deposition chamber. The NPs were deposited onto two different kinds of substrates: an amorphous carbon-coated Cu grid and a single crystal Si wafer. A Ti capping layer was deposited onto Fe NPs collected on Si substrate to protect Fe NPs from oxidation. However, no capping layer was deposited for Fe NPs collected on the Cu grid which was used for transmission electron microscopy (TEM) characterization.

In order to control the growth and phase formation of Fe NPs, field-controlled plasma-heating effects were promoted. As shown in Fig. 1, magnetic field intensity was modified by varying Cu disk thickness behind the Fe target. The magnetic field distribution was adjusted with the Fe ring and cone [27,28]. In our GPC system, NPs are formed from a high-temperature phase to a low-temperature phase following the thermal gradient induced by plasma. The plasma region depends on sputtering current I and magnetic field intensity B. Different I and B can form longer or shorter plasma regions as shown in Fig. 1. In the case of a high current and small magnetic field, the plasma region is long because of the higher cathode accelerating voltage and less plasma confinement from small magnetic field (dashed line in Fig. 1). By contrast, low current and large magnetic field can induce a short plasma region (solid line in Fig. 1). At the edge of the plasma region (black solid line and dashed line in Fig. 1), Fe NPs quench down dramatically due to the lack of energy source. This means that the plasma boundary behaves as the quench boundary for Fe NPs. By changing the current and magnetic field, the plasma region stretches back and forth. Accordingly, Fe NPs can quench at a certain intermediate phase like the bct phase. As shown in Fig. 1, under the condition of high current and small magnetic field (I_1, B_1), the plasma region is long and Fe NPs have more time to gradually cool to the bcc Fe phase. When low current and high magnetic field (I_2, B_2) are applied, bct Fe NPs start to form. In this paper, bcc Fe NPs were prepared using $I_1 = 0.6$ A and $B_1 = 700$ G and bct Fe NPs were obtained using $I_2 = 0.2$ A and $B_2 = 850$ G.

Several characterization methods were used to investigate the phase information, morphology, and magnetic properties of Fe NPs. The phase of Fe NPs was characterized by XRD and high-resolution transmission electron microscopy (HRTEM). The convergent-beam electron diffraction (CBED) imaging technique was used to further confirm the phase information. Elemental analysis was performed by scanning TEM energy-dispersive x-ray spectroscopy (STEM-EDS). Magnetic hysteresis loop measurements were done with a magnetic properties measurement system (MPMS) at temperatures ranging from 5 K to 300 K.

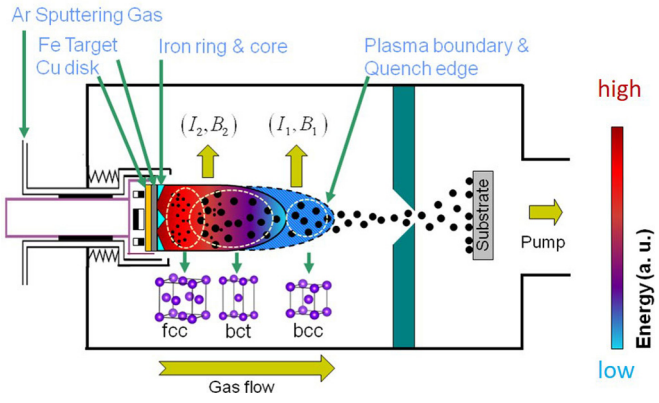

FIG. 1. Schematic diagram of Fe nanoparticle synthesis system, integrated with the illustration for the concept of tuning the thermal history for the growth of bcc and bct Fe nanoparticles. Setting the sputtering current $I_1 > I_2$ and the surface magnetic field at the target $B_1 < B_2$, the plasma region is longer for (I_1, B_1) than for (I_2, B_2), resulting in two different spatial quenching boundaries shown as a dotted line and a solid line. Varying I and B, different phases of Fe NPs can be obtained.

III. RESULTS AND DISCUSSION

A. Structure and morphology analysis

In order to get the evidence of the tetragonal distorted phase of Fe NPs, the XRD pattern is collected as shown in Fig. 2. Three diffraction peaks with approximately equal proportions centered around the bcc Fe (110) are observed. These adjacent peaks match well with the bcc Fe and tetragonal distorted bcc Fe phase. CrystalMaker software is used to simulate diffraction patterns for bcc and bct Fe. A bcc Fe structure is simulated using a standard database as a control pattern. And a bct Fe structure is also simulated using lattice constants of $a = 2.75$ Å and $c = 3.38$ Å ($c/a = 1.23$), determined from the XRD pattern assuming a tetragonal crystal structure. The simulated diffraction peaks match well with the experimental data, indicating that the sample contains the bct Fe phase. From the XRD pattern, some bcc Fe NPs still exist in the Fe NP sample, which is due to the inhomogeneous quenching effects along the etching track of the Fe target. The diffraction peak around $2\theta = 69^\circ$ is from the Si substrate. Small diffraction peaks around 48° and 49° originate from the oxidation of the

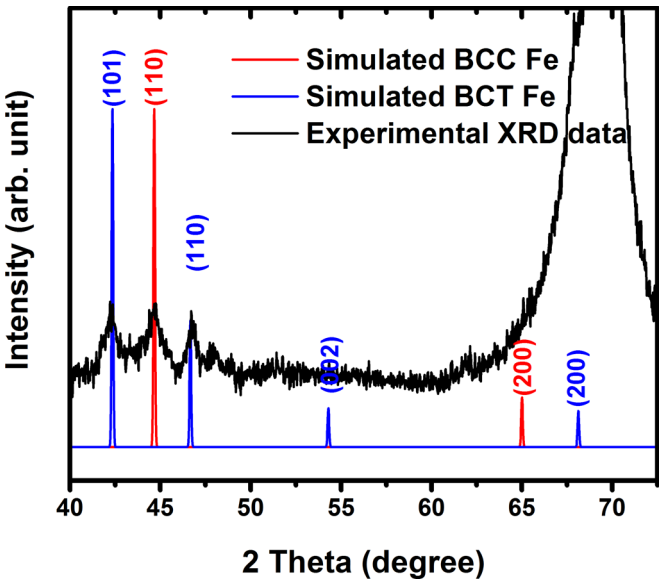

FIG. 2. XRD patterns of Fe NPs formed at $I_2 = 0.2$ A and $B_2 = 850$ G. The black line, blue line, and red line are the diffraction pattern of experimental results, simulated bct Fe diffraction peaks, and simulated bcc Fe peaks, respectively.

capping layer. Moreover, no iron oxide diffraction peaks are observed. Phase characterization of the bcc Fe NP sample can be found in the Supplemental Material [29].

In order to obtain further information on bct Fe NPs, the morphology and structure of the Fe NPs are investigated using HRTEM operated at 300 keV for bright-field imaging and diffraction patterns are operated at 100 keV (to mitigate beam damage on NPs) for the CBED imaging. The size distribution of NPs is estimated using TEM with lower magnification. The size of NPs follows a Gaussian distribution with 12 nm average size and 2.6 nm standard deviation. Both polyhedral and cubic NPs are found as shown in Fig. 3(a). The cubic NPs are bcc Fe and more information on this can be found in the Supplemental Material [29]. The crystallinity of polyhedral particles is demonstrated by high-resolution bright-field imaging as shown in Fig. 3(b), where a shell of the Fe NP is observed due to the oxidation of Fe NPs (see elemental analysis in the Supplemental Material [29]). Indexing the core lattice fringes is done by comparing the fast Fourier transform (FFT) of the region within the red box to a diffraction pattern simulated by CrystalMaker software. The forbidden peaks in FFT are also accounted for during the comparison. The standard method of indexing these patterns is done by comparing diffraction vector ratios, g_1/g_2, and angles, θ, with those of known phases and orientations. The ratio and angles shown in Fig. 3(c) match poorly with a bcc structure so they are compared with a bct structure simulated with lattice constants determined from the XRD pattern. The FFT pattern is matched well with a [131] zone axis pattern of the bct Fe structure. To further characterize the polyhedral particles, CBED analysis is carried out on a single polyhedral NP, as shown in Fig. 3(d). The CBED pattern is compared with the simulated diffraction pattern of bcc Fe structure. Again, no diffraction ratios or angles of the bcc structure match with the experimental CBED pattern. A main feature of the CBED pattern is that the angle between diffraction peaks is not 90°, as would be expected for a bcc Fe. The simulated bct structure determined from XRD pattern, not shown here, matches better with the CBED pattern than the bcc structure. However, it is still not within the error of our measurements. The deviation of our simulated bct pattern based on the XRD results can be understood by considering the nonuniformity of the Fe NPs. Certain NPs may have different lattice constants depending on their local strain. To improve our simulated bct Fe diffraction pattern, the experimental lattice constants are calculated directly from the CBED pattern shown in Fig. 3(d). The new diffraction pattern simulated using these calculated values is shown in Fig. 3(f). As shown in Figs. 3(e) and 3(f), the NP CBED pattern shown in Fig. 3(d) is not consistent with a bcc Fe structure; however, good agreement is achieved assuming a bct Fe structure.

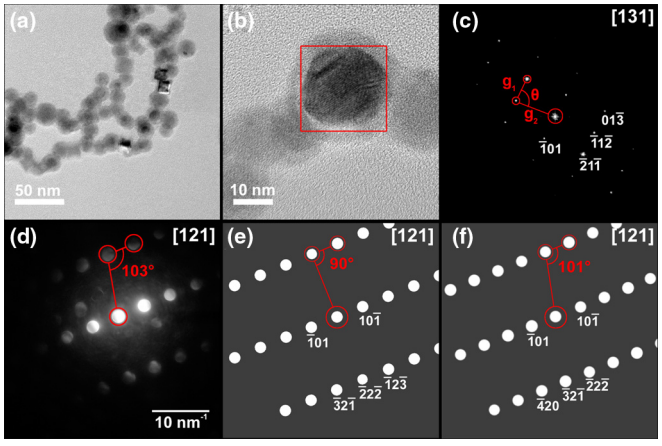

FIG. 3. TEM images of Fe NPs formed by GPC. (a) Bright-field image of polyhedral and cubic Fe NPs. (b) HRTEM image of polyhedral Fe NPs. (c) FFT of the red square in (b) (where g_1, g_2, and θ are two diffraction vectors and the angle between them, respectively). (d) Convergent beam electron diffraction (CBED) pattern of a single polyhedral Fe NP. Panels (e) and (f) show simulated diffraction patterns for bcc and bct Fe crystal structures.

B. Magnetic characterization

Hysteresis loops are measured to demonstrate the high MAE of bct Fe NPs. Magnetic in-plane (IP) and out-of-plane (OP) hysteresis loops of the bct Fe NP sample are shown in Figs. 4(a) and 4(b), respectively. Applied magnetic field is parallel to the substrate for IP loops and perpendicular for OP loops. IP loops show that the bct Fe NP sample has coercivity of 1.04×10^5 A/m at 300 K and 3.22×10^5 A/m at 5 K. As an experiment control, a bcc Fe NP sample is also prepared and the coercivity of the bcc Fe NP sample is 0.60×10^5 A/m at 300 K and 0.96×10^5 A/m at 5 K as shown in Fig. 4(c). From the TEM images shown in Fig. 3(a), Fe NPs have in-plane chain structures, which may enhance the coercivity of IP loops [21,22]. Therefore, OP loops are also measured to differentiate shape anisotropy from magnetocrystalline anisotropy. As shown in Fig. 4(b), OP loops have coercivity of 0.92×10^5 A/m at 300 K and 2.74×10^5 A/m at 5 K, which are both slightly smaller than that of IP loops. OP hysteresis loops of the bcc Fe NP sample are also measured with coercivity 0.42×10^5 A/m at 300 K and 0.73×10^5 A/m at 5 K as shown in Fig. 4(d). The bct Fe NP sample shows higher coercivity for

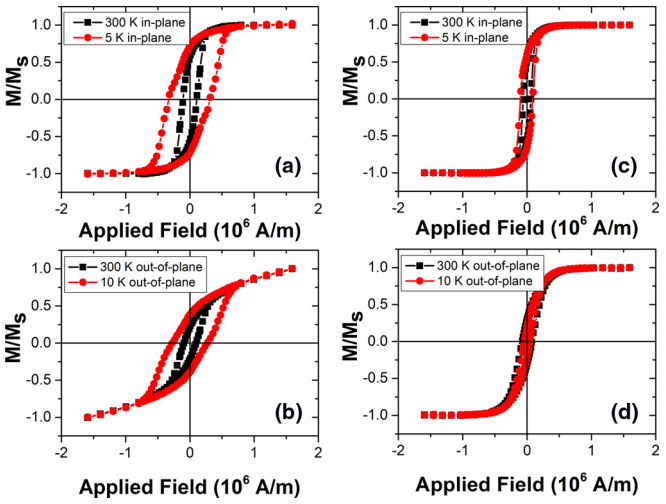

FIG. 4. The hysteresis loops of the bct Fe NP sample and bcc Fe NP sample. (a) bct Fe NP sample in-plane hysteresis loops, and (b) bct Fe NP sample out-of-plane loops. (c) bcc Fe NP sample in-plane hysteresis loops, and (d) bcc Fe NP sample out-of-plane hysteresis loops.

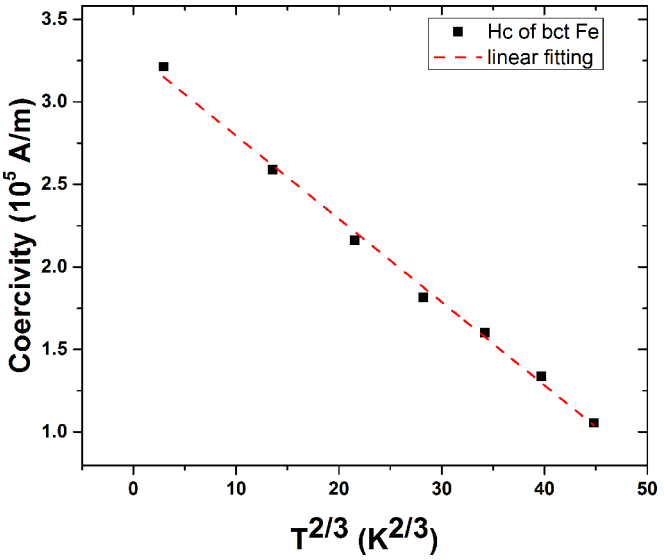

FIG. 5. Temperature-dependent coercivity of bct Fe NP sample, where black squares stand for experimental data and red dashed line is the fitting curve based on Eq. (1).

both IP and OP loops than that of bcc Fe NPs, indicating that bct Fe NPs have higher MAE. Although NP chains can increase the coercivity slightly, the main reason for the high coercivity of the bct Fe NP sample is due to high magnetocrystalline anisotropy from the tetragonal phase.

The M_s of the bct Fe NP sample can be estimated using the hysteresis loops measured by MPMS and TEM images, which allow us to obtain the magnetic moment and NP volume of the sample, respectively. The NP coverage ratio on the silicon substrate is assumed to be the same as that for the TEM sample. Therefore, the total volume of NPs is estimated using the coverage ratio, the mean size of NPs, and the area of the silicon substrate. Using these assumptions, the M_s of bct Fe at 5 K is $(1.6 \pm 0.4) \times 10^6$ A/m $(2.2 \pm 0.5\,\mu_B/\text{atom})$. The error bar for M_s is from the size and the coverage ratio variation of NPs. The M_s of bcc Fe is also estimated using the same method and the mean value of M_s is similar to that of the bct Fe NPs sample.

The bct/bcc Fe ratio can also be estimated using 5 K IP hysteresis loops as shown in Fig. 4. Small kinks are in the second quadrant with M/M_s ranging from 0.52 to 0.18. The kinks indicate there are two phases in the sample, bcc and bct Fe. The bct Fe shows higher coercivity compared to bcc Fe. Since the M_s values of bcc Fe and bct Fe are similar, the bct Fe phase ratio can be estimated in a range between 46% and 84% (see the Supplemental Material [29]).

The magnetocrystalline anisotropy K_u of the bct Fe NP sample is estimated by its temperature-dependent coercivities. Hysteresis loops are measured at temperatures ranging from 5 K to 300 K. Coercivity decreases as the temperature increases due to thermal fluctuation. K_u can be derived from the Sharrock equation using temperature-dependent coercivities [30,31]:

$$H_c(T) = H_0 - H_0\left[\frac{k_B}{K_u V}\ln(f_0 t)\right]^{\frac{2}{3}} T^{\frac{2}{3}}, \qquad (1)$$

where $H_c(T)$ represents coercivity at different temperature, H_0 is the coercivity at 0 K, k_B is Boltzman's constant, V is the volume of the bct phase NP, f_0 is the attempted frequency $\sim 10^9$ Hz, and t is the measure time ($\sim$ 5 sec). Here the exponent 2/3 is used for the Sharrock equation due to the magnetic interactions and easy-axis distribution of NPs. Figure 5 shows the experimental data and fitting curve based on Eq. (1) and the fitting result matches the experimental data very well. Based on the linear relationship between coercivity and $T^{2/3}$, $K_u V$ is estimated as $\sim 1.63 \times 10^{-19}$ J. Since the size of NPs is smaller than 100 nm as shown in Fig. 3, the Scherrer equation is used to estimate the average grain size of bct Fe NPs using XRD patterns as shown in Fig. 2 [32]. The bct Fe crystal size ranges from 9.8 nm to 11.6 nm. Therefore, the magnetocrystalline anisotropy can be estimated as $K_u \sim (2.65 \pm 0.67) \times 10^5$ J/m^3 $[(21.2 \pm 5.3)\,\mu$eV/atom], which is around seven times higher than that of bcc Fe, 4.8×10^4 J/m^3 $(3.5\,\mu$eV/atom).

IV. CONCLUSION

In conclusion, polyhedral Fe NPs with large coercivity and high-saturation magnetization have been successfully synthesized with a GPC method. The large coercivity is attributed to a strain-induced tetragonal bct Fe phase, which has higher magnetocrystalline anisotropy compared with bcc Fe. Initial XRD characterization shows a peak splitting which is consistent with a tetragonal distortion of bcc Fe. High-resolution TEM lattice fringe indexing and CBED pattern analysis also demonstrate the bct phase of these NPs. With this evidence, it is hypothesized that these polyhedral Fe NPs are an experimental demonstration of the metastable bct Fe phase predicted by first-principle calculations. Future work will further confirm the absolute lattice constants and phase of these NPs as well as more comprehensively determine the NP size, NP interaction, and strain effects on the magnetic properties of the NPs. This work proves the feasibility of the formation of highly strained polyhedral Fe NPs which are promising candidates for future non-rare-earth permanent magnetic materials.

ACKNOWLEDGMENTS

This work was partially supported by ARPA-E (Advanced Research Projects Agency-Energy) BCT $Fe_{16}N_2$ Magnet project under Contract No. 0472-1595), and parts of this work were carried out in the Characterization Facility, University of Minnesota, which receives partial support from NSF through the MRSEC program under Award No. DMR-1420013. The authors acknowledge partial support from the Institute for Rock Magnetism, Department of Earth Science, University of Minnesota, Twin Cities, for the use of instruments.

J.L. and K.S. contributed equally to this work. J.L., S.-H.H., and J.-P.W. designed the experiment. J.L. and S.-H.H. fabricated the sample and measured the XRD, TEM, and hysteresis loops. K.S. performed the HRTEM, CBED, and STEM characterization and contributed to the Fe phase analysis and the manuscript preparation. D.F. contributed to the TEM analysis. B.M. contributed to the data analysis. Y.J. did part of the NP sample synthesis and analysis. J.-P.W. initialized and coordinated the whole project. J.L. and J.-P.W. drafted the manuscript, and all co-authors commented on the manuscript.

[1] S. Chu and A. Majumdar, Nature (London) **488**, 294 (2012).
[2] J. M. D. Coey, J. Magn. Magn. Mater. **248**, 441 (2002).
[3] L. H. Lewis and F. Jiménez-Villacorta, Metall. Mater. Trans. A **44A**, 2 (2012).
[4] M. J. Kramer, R. W. McCallum, I. A. Anderson, and S. Constantinides, JOM **64**, 752 (2012).
[5] X. Liu, S. He, J.-M. Qiu, and J.-P. Wang, Appl. Phys. Lett. **98**, 222507 (2011).
[6] S.-H. Hung and K. McKenna, Phys. Rev. Mater. **1**, 24405 (2017).
[7] R. C. Hall, J. Appl. Phys. **31**, S157 (1960).
[8] K. Umemoto, B. Himmetoglu, J.-P. Wang, R. M. Wentzcovitch, and M. Cococcioni, J. Phys. Condens. Matter **27**, 016001 (2015).
[9] T. Burkert, O. Eriksson, P. James, S. I. Simak, B. Johansson, and L. Nordström, Phys. Rev. B **69**, 104426 (2004).
[10] T. Burkert, L. Nordström, O. Eriksson, and O. Heinonen, Phys. Rev. Lett. **93**, 027203 (2004).
[11] H. Jenniches, J. Shen, C. V. Mohan, S. S. Manoharan, J. Barthel, P. Ohresser, M. Klaua, and J. Kirschner, Phys. Rev. B **59**, 1196 (1999).
[12] K. Heinz, S. Müller, and L. Hammer, J. Phys.: Condens. Matter **11**, 9437 (1999).
[13] M. Weinelt, S. Schwarz, H. Baier, S. Müller, L. Hammer, K. Heinz, and T. Fauster, Phys. Rev. B **63**, 205413 (2001).
[14] R. Vollmer and J. Kirschner, Phys. Rev. B **61**, 4146 (2000).
[15] Q.-f Zhan, S. Vandezande, K. Temst, and C. Van Haesendonck, Phys. Rev. B **80**, 094416 (2009).
[16] V. Martin, W. Meyer, C. Giovanardi, L. Hammer, K. Heinz, Z. Tian, D. Sander, and J. Kirschner, Phys. Rev. B **76**, 205418 (2007).
[17] G. Andersson, T. Burkert, P. Warnicke, M. Björck, B. Sanyal, C. Chacon, C. Zlotea, L. Nordström, P. Nordblad, and O. Eriksson, Phys. Rev. Lett. **96**, 037205 (2006).
[18] M. Gong, A. Kirkeminde, M. Wuttig, and S. Ren, Nano Lett. **14**, 6493 (2014).
[19] S. S. Saxena and P. B. Littlewood, Nature (London) **412**, 290 (2001).
[20] E. C. Bain, Trans. Am. Inst. Mining, Metall. Pet. Eng. **70**, 25 (1924).
[21] J.-M. Qiu and J.-P. Wang, Adv. Mater. **19**, 1703 (2007).
[22] Y.-H. Xu and J.-P. Wang, Adv. Mater. **20**, 994 (2008).
[23] Y. Jing, S. He, and J. Wang, IEEE Trans. Magn. **49**, 197 (2013).
[24] J. Liu, K. Wu, and J. P. Wang, AIP Adv. **6**, 56126 (2016).
[25] Jian-Ping Wang, Proc. IEEE **96**, 1847 (2008).
[26] X. Liu and J.-P. Wang, J. Appl. Phys. **105**, 07A722 (2009).
[27] J.-M. Qiu and J.-P. Wang, Appl. Phys. Lett. **88**, 192505 (2006).
[28] S. He, Y. Jing, and J. Wang, J. Appl. Phys. **113**, 134310 (2013).
[29] See Supplemental Material at http://link.aps.org/supplemental/10.1103/PhysRevMaterials.2.054415 for a detailed description of phase characterization of bcc Fe NPs, element analysis of bct Fe NPs, bct Fe phase ratio calculation, and K_u estimation.
[30] M. P. Sharrock, IEEE Trans. Magn. **35**, 4414 (1999).
[31] J. Bai, Y.-H. Xu, J. Thomas, and J.-P. Wang, Nanotechnology **18**, 65701 (2007).
[32] A. A. El-Gendy, M. Qian, Z. J. Huba, S. N. Khanna, and E. E. Carpenter, Appl. Phys. Lett. **104**, 023111 (2014).